

1 **Implications of grain-size evolution on the seismic structure of the oceanic**
2 **upper mantle**

3 Mark D. Behn (corresponding author)

4 *Department of Geology and Geophysics, Woods Hole Oceanographic Institution, 360 Woods Hole Road- MS #22,*
5 *Woods Hole, MA 02543 USA; Phone: 508-289-3637; Fax: 508-457-2187; mbehn@whoi.edu*

6 Greg Hirth

7 *Department of Geological Sciences, Brown University, Providence, RI, 02912, USA; Phone: 401-863-7063; Fax:*
8 *401-863-2058; Greg_Hirth@brown.edu*

9 James R. Elsenbeck, II

10 *MIT/WHOI Joint Program in Oceanography, Woods Hole Oceanographic Institution, Woods Hole, MA 02543 USA*

11
12 **Abstract:** We construct a 1-D steady-state channel flow model for grain size evolution in the
13 oceanic upper mantle using a composite diffusion-dislocation creep rheology. Grain size
14 evolution is calculated assuming that grain size is controlled by a competition between dynamic
15 recrystallization and grain growth. Applying this grain size evolution model to the oceanic upper
16 mantle we calculate grain size as a function of depth, seafloor age, and mantle water content.
17 The resulting grain size structure is used to predict shear wave velocity (V_S) and seismic quality
18 factor (Q). For a plate age of 60 Myr and an olivine water content of 1000 H/10⁶Si, we find that
19 grain size reaches a minimum of ~15 mm at ~150 km depth and then increases to ~20–30 mm at
20 a depth of 400 km. This grain size structure produces a good fit to the low seismic shear wave
21 velocity zone (LVZ) in oceanic upper mantle observed by surface wave studies assuming that the
22 influence of hydrogen on anelastic behavior is similar to that observed for steady state creep.
23 Further it predicts a viscosity of ~10¹⁹ Pa s at 150 km depth and dislocation creep to be the
24 dominant deformation mechanism throughout the oceanic upper mantle, consistent with
25 geophysical observations. We predict larger grain sizes than proposed in recent studies, in which
26 the LVZ was explained by a dry mantle and a minimum grain size of 1 mm. However, we show
27 that for a 1 mm grain size, diffusion creep is the dominant deformation mechanism above 100–
28 200 km depth, inconsistent with abundant observations of seismic anisotropy from surface wave
29 studies. We therefore conclude that a combination of grain size evolution and a hydrated upper
30 mantle is the most likely explanation for both the isotropic and anisotropic seismic structure of
31 the oceanic upper mantle. Our results also suggest that melt extraction from the mantle will be
32 significantly more efficient than predicted in previous modeling studies that assumed grain sizes
33 of ~1 mm.

34 **Key Words:** asthenosphere, grain size, oceanic upper mantle, seismic low velocity zone.

35 1. Introduction

36 Grain size is a key microstructural property of the Earth's mantle, because it influences
 37 rheology, deformation mode (e.g., diffusion vs. dislocation creep), seismic attenuation and wave-
 38 speeds, electrical conductivity, and melt permeability. However, due to the lack of direct
 39 constraints, and because grain size evolves in response to the surrounding flow field, little is
 40 known about the distribution of grain size in the upper mantle. While grain size is often
 41 estimated using a piezometric relationship, in which grain size is directly related to stress (e.g.,
 42 *Twiss, 1977; Karato et al., 1980; van der Wal, 1993*), more recent studies have proposed models
 43 in which grain size evolution is also sensitive to temperature and strain rate (*de Bresser et al.,*
 44 *2001; Hall & Parmentier, 2003; Montési & Hirth, 2003; Austin & Evans, 2007*). However, to
 45 date these evolutions laws have not been incorporated in large-scale models of mantle flow,
 46 despite the potential importance of feedbacks between grain-size, rheology, and deformation.

47 Accurate estimates of grain size are important for interpreting upper mantle seismic structure.
 48 Laboratory data show that in addition to the well-known temperature-dependence of shear-wave
 49 speed (V_s) and attenuation (Q) (*Minster & Anderson, 1981*), V_s and Q are also sensitive to grain
 50 size (*Tan et al., 2001; Cooper, 2002; Jackson et al., 2002*). By extrapolating these data to upper
 51 mantle conditions the commonly observed low shear wave velocity zone (LVZ) beneath the
 52 ocean basins (e.g., *Gutenberg, 1948*) (Figure 1) can be explained by variations in grain size
 53 without requiring the presence of melt, H₂O, and/or compositional variations (*Faul & Jackson,*
 54 *2005*). The origin of the LVZ is important for understanding global mantle convection, because
 55 this zone is thought to represent a region of low viscosity, which accommodates plate motions
 56 and promotes plate tectonics (*Richards et al., 2001*). However, it is not clear whether the
 57 variation in grain size from 1 to 50 mm between 150 and 300 km depth required by *Faul &*
 58 *Jackson (2005)* is consistent with the deformation field in the upper oceanic mantle, and thus
 59 whether other factors such as water and/or melt are required to explain the LVZ.

60 Grain size also modulates the anisotropic structure of the upper mantle by affecting the
 61 relative rates of diffusion and dislocation creep. Deformation by diffusion creep occurs via
 62 diffusion of atoms along grain boundaries and produces a randomly aligned crystallographic
 63 fabric that is seismically isotropic. In contrast, dislocation creep occurs via slip along
 64 crystallographic planes, creating a preferred alignment of mineral grains, referred to as lattice

Fig. 1

65 preferred orientation (LPO). Olivine, the dominant phase in the Earth's upper mantle, is highly
66 anisotropic, with a fast P-wave velocity (and shear wave polarization) direction oriented parallel
67 to the crystallographic [100] axis (*Birch*, 1960, 1961; *Verma*, 1960). Thus, the crystallographic
68 alignment of olivine crystals by dislocation creep produces an anisotropic fabric that can be
69 measured using a variety of seismic techniques.

70 The relationship between seismic anisotropy and mantle flow is seen most clearly in the
71 ocean basins, where observations of azimuthal anisotropy near the East Pacific Rise (*Wolfe &*
72 *Solomon*, 1998; *Harmon et al.*, 2004) and in young Pacific upper mantle (*Nishimura & Forsyth*,
73 1989; *Montagner & Tanimoto*, 1991; *Becker et al.*, 2003; *Gaboret et al.*, 2003; *Conrad et al.*,
74 2007) are consistent with mantle flow in the direction of plate motion. Moreover, surface wave
75 models indicate that the depth of strongest radial anisotropy increases with age beneath the ocean
76 basins and corresponds to the center of the asthenosphere where shear flow is focused
77 (*Nishimura & Forsyth*, 1989; *Gaherty et al.*, 1996; *Nettles & Dziewonski*, 2008). Using a
78 composite diffusion-dislocation creep rheology to model deformation in the oceanic upper
79 mantle, *Podolefsky et al.* (2004) showed that the observed anisotropic structure is consistent with
80 the depth range over which deformation is dominated by dislocation creep. However, this model
81 assumed a constant grain size and thus did not account for grain size evolution associated with
82 mantle flow.

83 The goal of this study is to quantify grain size evolution in the oceanic upper mantle and
84 determine the influence of the resulting grain size distribution on seismic structure. We model
85 deformation in the upper mantle using a 1-D channel flow model that incorporates a composite
86 diffusion-dislocation creep rheology. Grain size evolution is calculated as a function of depth,
87 seafloor age, and mantle water content using the scaling relations of *Austin & Evans* (2007). The
88 resulting grain size profile is then used to predict the isotropic and anisotropic seismic structure
89 of the oceanic upper mantle as a function of seafloor age. For a plate age of 60 Myr and a dry
90 mantle (50 H/10⁶Si in olivine), we find that grain size reaches a minimum of ~5 mm at ~150 km
91 depth and increasing to only ~8 mm at a depth of 400 km. The magnitude of this variation in
92 grain size with depth is significantly smaller than that required in the end-member model used by
93 *Faul & Jackson* (2005) to explain the oceanic LVZ without the presence of water and/or melt.

94 However, if the mantle contains 1000 H/10⁶Si in olivine the predicted seismic structure is
 95 consistent with both the LVZ and the presence of radial anisotropy in the oceanic upper mantle.

96 2. 1-D Channel Flow Model for Grain Size Evolution

97 2.1 Model Setup

98 We simulate deformation in the oceanic upper mantle using a 1-D channel flow model
 99 following the approach of *Podolefsky et al.* (2004). Flow within the channel is driven by an
 100 imposed plate velocity, U_p , at the surface and zero velocity at a depth, $z = z_o$ (Figure 2).
 101 Assuming no horizontal pressure and viscosity gradients, shear stress within the channel is
 102 constant and a function of only the viscosity structure and the vertical gradient of horizontal
 103 velocity,

$$104 \quad \tau = \eta \frac{\partial u}{\partial z} \quad (1)$$

105 where τ is the shear stress, η is viscosity, and u is the horizontal velocity. Integrating Eq. (1)
 106 over the height of the channel allows us to write stress in terms of the plate velocity,

$$107 \quad \tau = U_p \left(\int_{z_o}^0 \frac{1}{\eta} dz \right)^{-1}. \quad (2)$$

108 Experimental and theoretical studies show that the rheology of an olivine aggregate follows a
 109 power-law relationship between stress and strain-rate (*Karato & Wu*, 1993; *Hirth & Kohlstedt*,
 110 2003),

$$111 \quad \dot{\epsilon}_i = A_i d^{-p_i} C_{OH}^{r_i} \tau^{n_i} \exp\left(-\frac{E_i + PV_i}{RT}\right) \quad (3)$$

112 where $\dot{\epsilon}_i$ is strain-rate, A_i is a material constant, p_i is the grain-size exponent, r_i is the water
 113 content exponent, n_i is the power-law exponent, E_i is the activation energy, V_i is the activation
 114 volume, R is the gas constant, d is the grain size, C_{OH} is the olivine water concentration (in
 115 H/10⁶Si), P is pressure, and T is temperature. The subscript i denotes the parameters that depend
 116 on the deformation mechanism (e.g., diffusion or dislocation creep). Flow law parameters are
 117 taken from *Hirth & Kohlstedt* (2003) and are given in Supplemental Table S1. We note that the
 118 pre-exponential constants for both diffusion and dislocation creep have been reduced by a factor

Fig. 2

119 of 3 relative to the values in *Hirth & Kohlstedt* (2003) based on the calibration for water content
 120 in olivine (*Bell et al.*, 2003).

121 Assuming that the total strain-rate can be expressed as the summation of the diffusion and
 122 dislocation components (e.g., *Parmentier et al.*, 1976),

$$123 \quad \dot{\epsilon} = \dot{\epsilon}_{diff} + \dot{\epsilon}_{disl} \quad (4)$$

124 we define an effective viscosity, η_{eff} , as

$$125 \quad \eta_{eff} = \left(\frac{1}{\eta_{diff}} + \frac{1}{\eta_{disl}} \right)^{-1} \quad (5)$$

126 which is controlled by the lower of the two viscosities. The conditions under which the
 127 dominant deformation mechanism switches between diffusion and dislocation creep are
 128 quantified through a transition stress, τ_T , defined as the stress for which $\dot{\epsilon}_{diff} = \dot{\epsilon}_{disl}$ (*Hall &*
 129 *Parmentier*, 2003; *Podolefsky et al.*, 2004).

130 2.2 Implementation of Grain Size Evolution Laws

131 Grain size in the Earth's mantle is controlled by the competition between dynamic
 132 recrystallization and static grain growth (*Karato*, 1984). During dynamic recrystallization,
 133 elastic strain energy is reduced by subgrain rotation and grain boundary bulging, producing
 134 smaller grains (*Twiss*, 1977; *Karato et al.*, 1980; *Poirier*, 1985; *van der Wal et al.*, 1993; *de*
 135 *Bresser et al.*, 1998). Grain size reduction can also occur via brittle processes (*Goodwin &*
 136 *Wenk*, 1995; *Bos & Spiers*, 2001; *de Bresser et al.*, 2001), however, for the high temperatures
 137 associated with asthenospheric flow these effects can be ignored. Grain growth occurs to reduce
 138 the interfacial energy of grain boundaries (*Urai et al.*, 1986; *Karato*, 1989; *Evans et al.*, 2001).
 139 Unlike dynamic recrystallization, which is only active in the dislocation creep regime, grain
 140 growth occurs in both the diffusion and dislocation regimes (*Karato & Wu*, 1993).

141 Grain size is frequently estimated using a piezometric relationship, in which grain size is
 142 related to only stress (e.g., *Karato et al.*, 1980; *Van der Wal et al.*, 1993). However, some
 143 experimental data suggests that grain size evolution is also sensitive to temperature and strain
 144 rate (e.g., *Poirier & Guillopé*, 1979; *de Bresser et al.*, 1998, 2001; *Drury*, 2005). Here we
 145 consider two models for grain size evolution: 1) the synchronous model of *Hall & Parmentier*

146 (2003), and 2) the paleowattmeter model of *Austin & Evans* (2007). Both of these models are
 147 based on the premise that grain size is controlled by the competition between grain growth and
 148 dynamic recrystallization:

$$149 \quad \dot{d} = \dot{d}_{gg} - \dot{d}_{dr} \quad (6)$$

150 where, \dot{d} , is the change in grain size with time, \dot{d}_{gg} is the rate of grain growth, and \dot{d}_{dr} is the rate
 151 of dynamic recrystallization.

152 *Hall & Parmentier* (2003) parameterized the change in grain size with time as

$$153 \quad \dot{d} = p_g^{-1} d^{1-p_g} G_o \exp\left(-\frac{E_g + PV_g}{RT}\right) - \lambda \dot{\epsilon}_{disl} d \quad (7)$$

154 where the two terms on the right hand side of the equation represent grain growth and
 155 recrystallization, respectively, G_o is the grain growth rate constant, E_g and V_g are the activation
 156 enthalpy and volume for grain growth, p_g is an experimentally determined grain growth constant,
 157 and λ provides an estimate of the strain necessary to achieve a new grain size. Eq. (6) can be
 158 solved for a steady state grain size, d_{ss} , which results when the rates of recrystallization and grain
 159 growth are balanced

$$160 \quad d_{ss} = \left(\frac{G_o}{p_g \lambda A_{disl}}\right)^{1/p_g} \left(\frac{\mu}{2\tau}\right)^{n_{disl}/p_g} \exp\left(\frac{(E_{disl} + PV_{disl}) - (E_g + PV_g)}{p_g RT}\right). \quad (8)$$

161 Here μ , is the shear modulus, and A_{disl} , n_{disl} , E_{disl} are the pre-factor, stress exponent, and activation
 162 energy for dislocation creep; the factor of 2 in front of the shear stress is necessary to convert to
 163 from shear to differential stress.

164 *Austin & Evans* (2007) proposed a similar model for grain size evolution based on the
 165 balance of mechanical work required for grain growth and dynamic grain size reduction. In
 166 practical terms, the primary difference between the *Austin & Evans* (2007) model and that
 167 proposed by *Hall & Parmentier* (2003), is that *Austin & Evans* (2007) assume changes in the
 168 internal energy of the system are proportional to grain boundary area and thus the time-scale for
 169 dynamic recrystallization scales as $\sim \tau \dot{\epsilon} d^2$ rather than $\sim \dot{\epsilon} d$ as in Eq. (7). The steady state grain
 170 size for the *Austin & Evans* (2007) model can then be approximated as

$$d_{ss} = \left(\frac{G_o \exp\left(-\frac{E_g + PV_g}{RT}\right) p_g^{-1} c \gamma}{2\tau\chi\dot{\epsilon}_{dist}} \right)^{\frac{1}{1+p_g}} \quad (9)$$

172 where γ is the average specific grain boundary energy, χ is the fraction of the work done by
 173 dislocation creep associated with changing grain boundary area, and c is a geometrical constant.
 174 Grain growth parameters for both models are given in Supplemental Table S2.

175 We calculate the steady state grain size with depth in our 1-D channel flow model assuming a
 176 fixed plate velocity, U_p , and mantle temperature structure. Temperature is calculated based on a
 177 half-space cooling model with a mantle potential temperature T_m and an adiabatic gradient of
 178 $0.3^\circ\text{C}/\text{km}$. To solve for grain size with depth we initially assume a uniform value of 1 mm
 179 throughout the model space and iterate to calculate stress following the approach of *Podolefsky*
 180 *et al.* (2004). We then use the resulting stress value to calculate a new grain size profile with
 181 depth using either Eq. (8) or (9). The new grain size profile is used to recalculate stress and the
 182 procedure is repeated until subsequent iterations change grain size by $< 1\%$.

183 2.3 Calibration of Grain Size Evolution Models to Laboratory Data

184 Before applying the *Hall & Parmentier* (2003) and *Austin & Evans* (2007) grain size
 185 evolution models to the upper mantle, we assessed their ability to reproduce laboratory data on
 186 grain size evolution during deformation experiments. Remarkably, the kinetics of grain growth
 187 remain poorly quantified. For example, analyzed grain boundary mobilities vary by > 3 orders
 188 of magnitude under laboratory conditions owing to differences in sample composition and the
 189 presence of residual porosity and/or melt (*Evans et al.*, 2001; *Faul & Scott*, 2006). Furthermore
 190 the activation enthalpy for grain growth has yet to be determined for dry, high-pressure
 191 conditions (*Karato*, 1989). However, grain size evolution models can still be tested using
 192 laboratory data on recrystallized grain size produced over a temperature range of 1100°C to
 193 1650°C (*Karato et al.*, 1980; *Van der Wal et al.*, 1993). Thus, our first test before applying the
 194 grain size evolution models to the Earth is to duplicate these laboratory results and in so doing
 195 generate a grain growth law that is consistent with the available data (c.f., *Austin & Evans*,
 196 2007).

197 We compare the *Hall & Parmentier* (2003) and *Austin & Evans* (2007) models to
 198 experimental data on wet (600 H/10⁶Si) and dry (50 H/10⁶Si) olivine (*Karato et al.*, 1980; *Van*
 199 *der Wal et al.*, 1993). To do this we modified the 1-D channel flow model described above to
 200 simulate laboratory conditions (e.g., constant pressure and temperature) and adjust strain-rate to
 201 evaluate the relationship between grain size and stress over a range of stresses. Flow laws for
 202 wet olivine aggregates (*Hirth & Kohlstedt*, 2003) and dry [101]_c olivine single crystals (*Bai et*
 203 *al.*, 1991) were used to simulate the experimental data of *Van der Wal et al.* (1993) and *Karato et*
 204 *al.* (1980), respectively. In all calculations we used the high-pressure grain growth data of
 205 *Karato* (1989).

206 For each model, we calculated the sensitivity of our results to the activation energy (E_g),
 207 activation volume (V_g) and grain growth exponent (p_g) (Figure 3). There is confusion in the
 208 literature regarding how to evaluate the sensitivity of kinetic laws to changes in the activation
 209 energy, volume, and/or stress exponent. Specifically, the co-variation of the pre-exponential
 210 terms with the other parameters is often ignored. Assuming a reference condition we can
 211 account for this co-variation in the grain growth laws by recalculating G_o after adjustment of E_g ,
 212 V_g and p_g

Fig. 3

$$213 \quad G_o = \frac{\left(G'_o \left(\frac{C_{OH}}{C_{OH(gref)}} \right) \exp \left(- \frac{E_{gref} + V_{gref} P_{gref}}{RT_{gref}} \right) t_{gref} + d_{gref}^{p_{gref}} \right)^{\frac{p}{p_{gref}}} - d_{gref}^p}{\exp \left(- \frac{E_g + V_g P_{gref}}{RT_{gref}} \right) t_{gref}} \quad (10)$$

214 where G'_o is the original value of the grain growth rate constant. Supplemental Table S2 gives
 215 the reference conditions and resulting values of E_g , V_g and p_g based on the grain growth
 216 parameters of *Karato* (1989) that we use in our models.

217 The grain sizes predicted by the *Austin & Evans* (2007) model using the high-pressure grain
 218 growth data (*Karato*, 1989) are systematically smaller than observed. As shown by *Austin and*
 219 *Evans* (2007), adequate fits to the data can be obtained by increasing G_o . This is justified by the
 220 presence of small amounts of porosity on the grain boundaries (resulting from fabrication of
 221 laboratory samples) that inhibit grain boundary mobility. By contrast, grain boundaries formed
 222 by dynamic recrystallization will not have pores. As stated above, no activation energy for grain

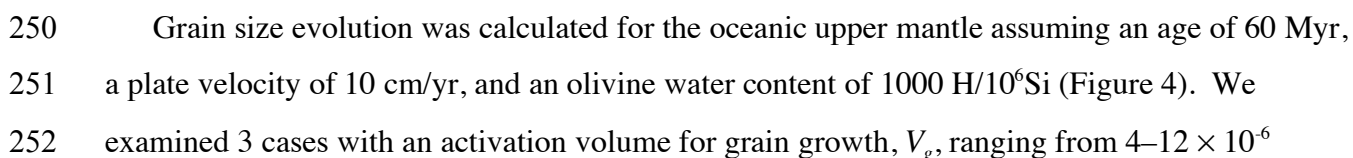
223 growth (at high pressure, dry conditions) is given in *Karato* (1989), thus we examined a range of
 224 values between 200 and 500 kJ/mol (Figure 3D). With $E_g = 350$ kJ/mol, G_o must be increased by
 225 a factor of ~ 180 compared to that determined in the dry experiments of *Karato* (1989) (Figure
 226 3D). A similar increase in G_o provides a good fit to the wet data (Figure 3B). Note that because
 227 a reference temperature of 1250°C was used, variations in activation enthalpy do not affect the
 228 model predictions for the wet olivine data, but strongly affect the predictions based on the dry
 229 olivine data that were collected at 1650°C.

230 Using the high-pressure grain growth parameters (G_o and E_g) of *Karato* (1989), we find that
 231 the *Hall & Parmentier* (2003) model systematically over-predicts grain size in the wet olivine
 232 data and under-predicts the dry olivine data (Figures 3A & 3C). In their original model, *Hall &*
 233 *Parmentier* (2003) used the grain growth parameters determined from the 1 atm experiments of
 234 *Karato* (1989). In these experiments grain growth was significantly inhibited due to the presence
 235 of residual porosity in the sample. Using the parameters derived from the 1 atm data would
 236 therefore further degrade the fit to the dry data, because the predicted grain size at a given stress
 237 would be smaller. This effect is even more pronounced at lower temperature. The fit to the dry
 238 data in Figure 3C could be improved by increasing G_o (similar to the approach of *Austin & Evans*
 239 (2007)). However, this would simultaneously degrade the fit to the wet data.

240 In summary, we find that the *Austin & Evans* (2007) model provides a better fit to the
 241 available data over a range of conditions than does the *Hall & Parmentier* (2003) model. Based
 242 on these results we use the *Austin & Evans* (2007) model for the remainder of this study,
 243 choosing values of $p_g = 3$ and $E_g = 350$ kJ/mol for both the wet and dry olivine data. While the
 244 laboratory data are equally well explained by $p_g = 2$ and $E_g = 500$ kJ/mol, a grain growth
 245 exponent of 3 is likely more relevant for mantle lithologies where grain boundary mobility is
 246 affected by grain boundary solutes (e.g., calcium and aluminum) [*Evans et al.*, 2001; *Hiraga et*
 247 *al.*, 2003]. Further, while E_g is not well constrained from laboratory data at high pressure, the
 248 limited data available indicate values less than 500 kJ/mol [*Karato*, 1989].

249 2.4 Application to the Oceanic Upper Mantle

250 Grain size evolution was calculated for the oceanic upper mantle assuming an age of 60 Myr,
 251 a plate velocity of 10 cm/yr, and an olivine water content of 1000 H/10⁶Si (Figure 4). We
 252 examined 3 cases with an activation volume for grain growth, V_g , ranging from 4–12 $\times 10^{-6}$


Fig. 4

253 m^3/mol . In all cases, grain size decreases rapidly from the surface to a depth ~ 100 km. This
 254 gradient is the result of the increase in strain-rate with depth beneath the thermal boundary layer.
 255 For the intermediate case of $V_g = 8 \times 10^{-6} \text{ m}^3/\text{mol}$, we find grain-size reaches a minimum of ~ 15
 256 mm at ~ 150 km depth, below which it increases slowly to ~ 22 mm at 400 km (Figure 4A). The
 257 predicted grain size and the magnitude of the variations with depth are somewhat larger for $V_g =$
 258 $4 \times 10^{-6} \text{ m}^3/\text{mol}$, while $V_g = 12 \times 10^{-6} \text{ m}^3/\text{mol}$ results in a monotonic decrease in grain size at all
 259 depths. The grain size profiles predict the asthenosphere to be dominated by dislocation creep
 260 down to at least ~ 400 km, which is consistent with the observation of radial anisotropy in the
 261 oceanic upper mantle (*Nishimura & Forsyth, 1989; Gaherty et al., 1996; Tan & Helmberger,*
 262 *2007; Nettles & Dziewonski, 2008*). However, greater values of V_g will push the dislocation-
 263 diffusion creep boundaries to shallower upper mantle depths. Plate velocity also influences
 264 grain-size, with slower velocities producing lower strain rates and thus larger grain-sizes (e.g., U_p
 265 = 1, 5, 10 cm/yr result in $d = 35, 21, 15$ mm at 150 km depth for $V_g = 8 \times 10^{-6} \text{ m}^3/\text{mol}$).

266 Eq. (7) can be used to determine the time scale over which the grain size evolves from an
 267 initial value, d_o , to the steady state value, d_{ss} (*Hall & Parmentier, 2003*). For all cases, the time-
 268 scale to achieve steady state is < 0.1 Myrs at depths below the base of the thermal boundary layer
 269 (~ 75 km) and are very small compared to the age of the plate (Figure 4D). This implies that in
 270 the absence of vigorous small-scale convection, the steady state value provides a good estimate
 271 of the grain size below the base of the lithosphere. To achieve a steady-state grain size in the
 272 lithosphere, however, requires times that are greater than the age of the plate and thus our
 273 calculations are not appropriate for estimating grain size in these regions (shown in grey in
 274 Figure 4). Furthermore, as olivine grain size approaches ~ 10 cm or greater, grain boundary
 275 pinning associated with the presence of secondary phases such as pyroxene likely control the
 276 maximum grain size (*Evans et al., 2001*).

277 All 3 activation volumes for grain growth (V_g) result in a mantle viscosity of $\sim 10^{19}$ Pa·s at the
 278 center of the asthenosphere increasing to $\sim 10^{20}$ – 10^{21} Pa·s at 400 km (Figure 4B). Because
 279 deformation is dominated by dislocation creep in all 3 cases (Figure 4C), the increase in viscosity
 280 with depth reflects the activation volume for dislocation creep. These values of asthenospheric
 281 viscosity are similar to estimates from post-seismic relaxation (*Pollitz & Sacks, 1996; Freed &*
 282 *Bürmann, 2004*) and geoid (*Craig & McKenzie, 1986; Hager, 1991*) studies, as well as

283 estimates of the viscosity at the base of the olivine stability field based on post-glacial rebound
 284 (*Peltier, 1998*).

285 To further test the sensitivity of our results, we examined the steady state grain size and
 286 mantle viscosity at a depth of 150 km as a function of mantle potential temperature and olivine
 287 water content (Figure 5). As expected elevated water contents result in larger grain sizes, due to
 288 the higher grain boundary mobility under hydrous conditions. Warmer temperatures also
 289 produce larger grain sizes. This occurs because higher temperatures promote grain growth,
 290 while simultaneously reducing asthenospheric viscosity, which in turn reduces the stress
 291 available to drive recrystallization. For example, at 150 km depth values of T_m of 1300, 1350,
 292 1400°C result in $d = 12, 15,$ and $22,$ respectively. Thus, for the range of potential temperatures
 293 and olivine water contents typical of the Earth's upper mantle (1300–1450°C and 50–2000
 294 H/10⁶Si), we find grain sizes and viscosities at the center of the asthenosphere in the range of 1–
 295 100 mm and 0.3–10 × 10¹⁹ Pa·s, respectively.

Fig. 5

296 Lastly, we tested the effect of imposing a rapid change in water content (50 to 1000 H/10⁶Si)
 297 at 70 km depth to simulate the dehydration boundary associated with the onset of dry melting
 298 beneath a ridge axis (*Hirth & Kohlstedt, 1996*). Intriguingly, our grain size profiles are
 299 essentially independent of a dehydration boundary for plate ages > 10 Myr, and are sensitive
 300 only to the water content of the mantle below 70 km. The reason for this can be seen from
 301 examination of Eq. (9), in which the steady state grain size is proportional to $C_{OH}^{p/p_{ref}} \dot{\epsilon}_{disl}^{-1}$. Just
 302 below the dehydration boundary there is a rapid increase in strain-rate due to the decrease in
 303 viscosity for wet olivine. However, the elevated water content below the dehydration boundary
 304 simultaneously enhances grain growth. These two effects almost perfectly offset in our simple
 305 1-D model, however future work is necessary to determine how these processes interact during
 306 corner flow beneath a ridge axis.

307 3. Seismic Structure of the Oceanic Upper Mantle

308 The resultant grain size profiles are used to calculate shear wave velocity (V_S) and seismic
 309 quality factor (Q) as a function of depth. Following *Karato (2003)*, we estimate V_S as:

$$310 \quad V_S = V_\infty(T, P) \left[1 - F \cdot Q^{-1}(\omega, T, P, C_{OH}, d) \right] \quad (11)$$

311 where ω is frequency, V_∞ is the velocity at infinite frequency, $F = (1/2) \cdot \cot(\pi\alpha/2)$ and α is a non-
 312 dimensional constant (Minster & Anderson, 1980). In this formulation, the influences of water
 313 and grain size on V_s enter through the anelastic term (enclosed in square brackets), while the
 314 effects of temperature and pressure influence both the anelastic and anharmonic terms. We
 315 calculate the velocity at infinite frequency, V_∞ , following *Stixrude & Lithgow-Bertelloni (2005)*:

$$316 \quad V_\infty(T, P) = 4.77 + 0.038P - 0.000378(T - 300) \quad (12)$$

317 in which pressure and temperature are given in GPa and °K, respectively. This expression
 318 incorporates the modal mineralogy of a pyrolytic bulk composition appropriate for the oceanic
 319 upper mantle.

320 The anelastic effects are approximated by:

$$321 \quad Q^{-1}(\omega, T, P, C_{OH}, d) = \left(B d^{-p_Q} \omega^{-1} \exp\left(-\frac{(E_Q + P V_Q)}{RT}\right) \right)^\alpha \quad (13)$$

322 where

$$323 \quad B = B_o d_{Qref}^{p_Q - p_{Qref}} \left(\frac{C_{OH}}{C_{OH(Qref)}} \right)^{r_Q} \exp\left(\frac{(E_Q + P_{Qref} V_Q) - (E_{Qref} + P_{Qref} V_{Qref})}{RT_{Qref}}\right). \quad (14)$$

324 The reference values, p_{Qref} , E_{Qref} , and V_{Qref} , are taken from *Faul & Jackson (2005)* and d_{Qref} , T_{Qref} ,
 325 P_{Qref} , and $C_{OH(Qref)}$ are given in Supplemental Table S3. To estimate the value of B consistent with
 326 Eq. (13) we fit the attenuation data of *Tan et al. (2001)* and *Jackson et al. (2002)* at a fixed
 327 period of 8.2 s with $\alpha = 0.27$. We find that $p_Q = 1$ and $E_Q = 420 \text{ kJ mol}^{-1}$ results in the best fit the
 328 data (Figure 6), consistent with *Faul & Jackson (2005)* and *Jackson et al. (2002)*, respectively.
 329 The resulting parameters for calculating Q and V_s are given in Supplemental Table S3. As
 330 hypothesized by *Karato (1995)*, the influence of hydrogen on attenuation is justified by the
 331 correlation between steady state creep rates and transient creep observed in deformation
 332 experiments (e.g., *Gribb & Cooper, 1998*). Exploratory experiments on hydrous olivine suggest
 333 that water can influence anelastic properties, but more quantitative analyses await further
 334 experimental work (*Aizawa et al., 2008*)

Fig. 6

335 Our approach for calculating V_s differs from *Faul & Jackson* (2005) in two ways. First, *Faul*
 336 *& Jackson* (2005) assumed a pure olivine upper mantle in their calculations of V_s . By utilizing
 337 the *Stixrude & Lithgow-Bertelloni* (2005) expression for V_∞ in Eq. (12) we account for the
 338 addition presence of pyroxene, garnet, and spinel, which can account for >30% of the oceanic
 339 upper mantle by volume. Second, unlike *Faul & Jackson* (2005), who allow grain size to
 340 influence both the anelastic and anharmonic terms (see Eq. (7) of *Faul & Jackson* (2005)), we
 341 include the grain-size dependence of V_s only in the anelastic term (Eq. 13) as grain size should
 342 not effect the unrelaxed properties of olivine. The net effect of our approach is to reduce the
 343 influence of grain size on V_s in our calculations as compared to those of *Faul & Jackson* (2005).

344 To assess the influence of grain size and olivine water content on V_s and Q , we compared
 345 two cases with grain-size profiles calculated for a dry (50 H/10⁶Si) and wet (1000 H/10⁶Si)
 346 mantle at 60 Myrs (Figure 7). Both cases result in V_s minima at a depth of ~130 km, which
 347 corresponds closely to the depth of the LVZ for intermediate oceanic plate ages (25–100 Myr)
 348 (e.g., *Nettles and Dziewonski*, 2008). Because the difference in water content has a greater effect
 349 on V_s than does the calculated change in grain size, the dry case predicts a slightly higher V_s
 350 (~4.4 km/s) at 130 km than does the wet case (~ V_s = 4.3 km/s). Comparing these results to
 351 available seismic models for the oceanic upper mantle we find that the wet case results in a
 352 slightly better fit to the observed LVZ. However, we note that there are considerable differences
 353 in the amplitude and depth of the LVZ between the seismic models resulting from the different
 354 spatial distribution and frequency content of the data used in constructing each model. Thus,
 355 given these uncertainties it is difficult to distinguish between the wet and dry cases from the
 356 seismic data alone.

Fig. 7

357 We also identify two discrepancies between our model predictions and the available
 358 constraints on the seismic structure of the upper oceanic mantle. First, our models predict a
 359 smaller velocity gradient at the base of the mantle than is observed (Figure 7B). One possible
 360 explanation for this difference is that we have underestimated V_Q in our calculations.
 361 Alternatively the composition of the mantle may not be constant near the transition zone.
 362 Second, the modeled V_s profiles lack the fast and constant velocity lid above 60–70 km depth
 363 that is observed in PA-5 (*Gaherty et al.*, 1996) and other recent studies that incorporate
 364 reverberation phases (e.g., *Tan & Helmberger*, 2007). The low temperatures (and associated

365 high Q values) in this depth range make it unlikely that the rapid change in V_S at the base of the
366 lid (also referred to as the Gutenberg or G- discontinuity) is generated by an anelastic mechanism
367 unless our thermal models vastly underestimate temperature at this depth. In the following
368 section we speculate on possible origins for the G-discontinuity in the oceanic upper mantle.

369 4. Discussion

370 We use our model to investigate the variation in upper mantle properties as a function of
371 oceanic plate age by examining a series of 1-D calculations with different imposed temperature
372 structures (Figure 8). While this approach ignores complications associated with buoyancy-
373 driven flow and ridge corner flow, it provides a first-order approximation of the variations in
374 upper mantle structure with age. A combination of petrological (*Dixon et al.*, 1988; *Michael et*
375 *al.*, 1995; *Hirth & Kohlstedt*, 1996; *Hirshmann et al.*, 2005) and geophysical observations (e.g.,
376 *Evans et al.*, 2005) indicate that there is 125 +/- 75 ppm by weight of water in the oceanic
377 mantle; this value results in approximately 1000 H/10⁶Si in olivine given the partition coefficient
378 of hydrogen between the mantle phases (*Hauri et al.*, 2006). Based on these observations, and
379 the fact that water content has only a limited influence on upper mantle grain size (Figures 5A &
380 Figure 7A), we consider a series of calculations with ~1000 H/10⁶Si and a mantle potential
381 temperature of 1350°C.

Fig. 8

382 For all plate ages, grain size is minimized at the depth corresponding to the maximum
383 dislocation creep strain rate. Further, the grain size at a given depth decreases with increasing
384 plate age, owing to the overall cooling of the mantle (Figure 8A). This positive gradient in grain
385 size from the center of the asthenosphere to the base of the upper mantle is consistent with that
386 proposed by *Faul & Jackson* (2005). However, the magnitude of the variations calculated from
387 our model are significantly smaller; for a plate age of 100 Myr we predict an increase from 15 to
388 22 mm between 150 and 400 km depth, while *Faul & Jackson* (2005) propose an increase on the
389 order of 1 to 50 mm. Although *Faul & Jackson* (2005) used a lower mantle potential
390 temperature (1300°C) than was considered here, we calculate a minimum grain size of 12 mm at
391 the center of the asthenosphere for 1300°C — still more than an order of magnitude larger than
392 their minimum grain size of 1 mm. As discussed below these differences have important
393 implications for the permeability and anisotropic structure of the upper mantle.

394 Grain sizes of 10–20 mm in the asthenosphere are consistent with available constraints on
 395 grain size in the upper mantle. Although few xenoliths from oceanic environments are available,
 396 xenoliths from continental extension zones, where upper mantle temperatures are likely be
 397 similar to those in the oceanic upper mantle, record grain sizes on the order of 1–20 mm (e.g.,
 398 *Ave Lallemant et al.*, 1980). Moreover, olivine in harzburgite and dunite bodies outside of
 399 mylonitic shear zones in the Oman ophiolite display grain sizes of 1–20 mm (*Boudier &*
 400 *Coleman*, 1981; *Braun*, 2004). While these grain sizes are slightly smaller than our predictions,
 401 the fabrics preserved in ophiolites are formed in the shallowest portions of the upper mantle,
 402 which is most strongly influenced by ridge corner flow, and have additionally undergone late
 403 stage deformation associated with exhumation. Finally, these estimates are generally consistent
 404 with previous inversions for grain size at 100 km depth and 1550°K from global attenuation
 405 models (*Cammarano & Romanowicz*, 2008), which suggest grain sizes of ~10 mm based on *Faul*
 406 *& Jackson's* (2005) parameterization for the effect of grain size on Q .

407 The calculated S-wave velocity structure predicts the depth of the low velocity zone (LVZ) to
 408 increase with increasing plate age, with the slowest velocities near the ridge axis where the
 409 shallow temperature structure is warmest (Figure 8B). Comparing the 1-D velocity structure at
 410 100 Myr with seismic models for old oceanic upper mantle, we find a good correspondence
 411 between the depth and minimum velocity of the LVZ (Figure 8D). We also calculated grain size
 412 and V_S at 100 Myr using temperatures derived from a plate-cooling model (*Parsons & Slater*,
 413 1977; *Stein & Stein*, 1992) assuming a plate thickness of 125 km and a mantle potential
 414 temperature of 1350°C (red curves in Figures 8C & 8D). The warmer temperatures calculated
 415 from the plate model produce slightly larger grain sizes and a slower, shallower LVZ compared
 416 to the half-space cooling model. However, again the available seismic constraints are not
 417 sufficient to distinguish between these two models and as discussed below neither model
 418 displays a fast, constant velocity lid above ~70 km.

419 The diffusion and dislocation creep rates calculated from the composite rheology (Eq. 4) can
 420 be used to infer the anisotropic structure of the oceanic upper mantle (Figure 9). Because
 421 anisotropy develops due to dislocation creep, but is destroyed (or at least does not form) in the
 422 diffusion creep regime, we assume that the mantle in our 1-D model will be strongly anisotropic
 423 when $\dot{\epsilon}_{dist} > \dot{\epsilon}_{diff}$ and $\epsilon_{dist} > 1$ (Figure 9C). Based on this criterion, we find that the maximum



424 depth-extent of anisotropy deepens with plate age, consistent with radial anisotropy models for
425 the Pacific derived from surface waves (e.g., *Nishimura & Forsyth, 1989; Nettles & Dziewonski,*
426 2008). However, while the peak amplitude of radial anisotropy increases slightly with plate age
427 in the ocean basins (e.g., Figure 1B), the coherence between azimuthal anisotropy and the fossil
428 seafloor fabric decays with age (*Nishimura & Forsyth, 1989*). This breakdown in coherence at
429 old ages is not predicted by our simple 1-D model in which flow is driven solely by ridge-normal
430 plate motion. Older regions of the oceanic mantle have likely experienced additional shear
431 associated with small-scale convection and/or larger-scale buoyancy-driven flow, which will
432 tend to re-align the orientation of shear in the asthenosphere relative to the fossil seafloor fabric.

433 For comparison, we also determined the region of the mantle dominated by dislocation creep
434 based on the grain size distribution of *Faul & Jackson (2005)*. To do this we used the composite
435 rheology to calculate stress and strain-rates in the upper mantle for a fixed grain size profile.
436 Assuming a linear increase in grain size from 1 to 50 mm between 165 and 350 km depth and a
437 mantle potential temperature of 1300°C as proposed by *Faul & Jackson (2005)*, we find that
438 diffusion creep is the dominant deformation mechanism above ~180 km (Figure 9F). Similarly,
439 their hot mantle grain size profile with a linear increase from 5 to 100 mm and $T_p = 1400^\circ\text{C}$,
440 predicts the upper 80 km of the mantle to be dominated by diffusion creep. Both of these models
441 are inconsistent with the observation of radial anisotropy in old oceanic upper mantle, and thus
442 argue that the minimum grain size in the oceanic upper mantle must be greater than 1–5 mm in
443 order to promote dislocation creep. Therefore, while our modeled grain size profiles are
444 consistent with the gradient in grain size in the upper oceanic model proposed by *Faul &*
445 *Jackson (2005)*, at face value directly inverting isotropic S-wave velocities for grain size at dry
446 conditions results in values that are inconsistent with the anisotropic velocity structure.

447 The largest discrepancy between the modeled and observed velocity structures is the inability
448 of our model to predict the high velocity lid above 60–70 km (G-discontinuity) for old ages that
449 is observed in reverberation phases (e.g., *Gaherty et al., 1996; Tan & Helmberger, 2007*). If this
450 high velocity lid is caused by anelastic effects, it would require a sharp change in mantle
451 properties at ~70 km depth that are not predicted by our model. Moreover, given the existing
452 thermal models for the oceanic upper mantle it is difficult to invoke an anelastic origin for the G-
453 discontinuity. To illustrate this point, we calculated the change in grain size or water content that

454 is required to produce a 3% decrease in velocity at 70 km as a function of mantle temperature
 455 (Figure 10). For relatively hot temperatures ($>1250^{\circ}\text{C}$) characteristic of young oceanic mantle,
 456 the variation in grain size (~ 10 mm) and/or water content (~ 2000 H/ 10^6 Si) needed to produce the
 457 G-discontinuity remains reasonable. However, for temperatures of 650° – 850°C predicted from
 458 half-space cooling at an age of 100 Myr lithosphere (the average age of PA-5) grain size and/or
 459 water content would have to vary by ~ 10 orders of magnitude in order to generate a 3% change
 460 in V_s (Figures 10A & 10B). In the case of water content, this would require values well above
 461 the solubility of water in olivine (*Zhao et al.*, 2004; Figure 10B&D). Furthermore, even the
 462 warmest published plate model (1400°C at 90 km; *Stein & Stein* (1992)) predicts a temperature
 463 of only $\sim 1100^{\circ}\text{C}$ at 70 km depth at 100 Myr, which would still require unreasonably large
 464 variations in grain size and/or water content to produce the G-discontinuity. Intriguingly, these
 465 warmer temperatures predicted from the *Stein & Stein* (1992) plate model do approach the damp
 466 (*Asimow et al.*, 2004) and carbonated (*Dasgupta & Hirshmann*, 2006) mantle solidi at 2–3 GPa,
 467 implying that melt could be present at these depths in old oceanic mantle. Thus, we conclude
 468 that either the temperature structure of old oceanic lithosphere is similar to or even hotter than
 469 the warmest published plate models, or an alternative mechanism such as compositional changes
 470 and/or scattering are required to explain the existence of the G-discontinuity.

471 The grain size profiles predicted by our model are also relevant for estimating the
 472 permeability of the oceanic mantle to melt migration. Melt permeability scales with d^2 (e.g., *von*
 473 *Bargen & Waff*, 1986; *Wark et al.*, 2003), thus an accurate estimate of grain size is necessary for
 474 determining the rate of melt migration. Some recent geodynamical studies have assumed
 475 permeabilities consistent with a mantle grain size of ~ 1 mm (e.g., *Braun et al.*, 2000; *Choblet &*
 476 *Parmentier*, 2001; *Spiegelman & Kelemen*, 2003; *Cagnioncle et al.*, 2007). However, our
 477 calculations predict minimum grain sizes of 10–20 mm, resulting in an increase in permeability
 478 by more than a factor of 100 compared to these previous studies. This will result in more rapid
 479 melt ascent velocities and in turn a smaller effect of melt buoyancy on mantle flow beneath
 480 ridges and plumes.

481 5. Conclusions

482 In this study, we have coupled laboratory based grain size evolution models with a 1-D
 483 channel flow model for the oceanic upper mantle assuming a composite diffusion-dislocation

484 creep rheology. We evaluated both the *Hall & Parmentier* (2003) and the *Austin & Evans*
485 (2007) grain size evolution models and found that the *Austin & Evans* (2007) model does a better
486 job at reproducing the available laboratory data over a range of experimental conditions (e.g.,
487 temperature and olivine water content). Applying the *Austin & Evans* (2007) model to the
488 oceanic upper mantle we find that for ages >60 Myr and an olivine water content of 1000
489 H/10⁶Si, grain size reaches a minimum of 15–20 mm at ~150 km depth, increasing to 20–30 mm
490 at 400 km. This grain size structure produces a good fit to the low seismic shear wave velocity
491 zone (LVZ) in oceanic upper mantle, and predicts dislocation creep to be the dominant
492 deformation mechanism at all depths throughout the upper mantle. Our results predict larger
493 grain sizes than proposed by *Faul & Jackson* [2005], who suggested that the LVZ could be
494 explained by a dry mantle and a minimum grain size of 1 mm. However, for a grain size of 1
495 mm diffusion creep is the dominant deformation mechanism above 100–200 km depth,
496 inconsistent with abundant observations of seismic anisotropy from surface wave studies. These
497 results indicate that a combination of grain size evolution and a hydrated upper mantle is a likely
498 explanation for the oceanic LVZ.

499 **6. Acknowledgements**

500 This work benefited from many fruitful discussions with Nick Austin, Brian Evans, Uli Faul,
501 Jim Gaherty, Dan Lizarralde, and Peter Kelemen. Careful reviews by Jim Gaherty and Uli Faul
502 and Rob van der Hilst (Editor) greatly improved this manuscript. Funding for this research was
503 provided by NSF Grants EAR-06-52707 and EAR-07-38880.

504

504 **7. References**

- 505 Aizawa, Y., Barnhoorn, A., Faul, U.H., Fitz Gerald, J.D., Jackson, I., Kovács, A.I., 2008, Seismic
 506 properties of Anita Bay Dunite: an exploratory study of the influence of water: *J. Petrology*,
 507 49, 841-855.
- 508 Asimow, P.D., Dixon, J.E., Langmuir, C.H., 2004, A hydrous melting and fractionation model for
 509 mid-ocean ridge basalts: Application to the Mid-Atlantic Ridge near the Azores: *Geochem.*,
 510 *Geophys.*, *Geosys.*, 5, Q01E16, doi:10.1029/2003GC000568.
- 511 Austin, N.J., Evans, B., 2007, Paleowattmeters: A scaling relation for dynamically recrystallized
 512 grain size: *Geology*, 35, 343-346.
- 513 Ave Lallemand, H.G., Mercier, J.-C.C., Carter, N.L., Ross, J.V., 1980, Rheology of the upper
 514 mantle: Inferences from peridotite xenoliths: *Tectonophys.*, 70, 85-113.
- 515 Bai, Q., Mackwell, S.J., Kohlstedt, D.L., 1991, High-temperature creep of olivine single crystals
 516 1. Mechanical results for buffered samples: *J. Geophys. Res.*, 96, 2441-2463.
- 517 Becker, T.W., Kellogg, J.B., Ekström, G., O'Connell, R.J., 2003, Comparison of azimuthal
 518 seismic anisotropy from surface waves and finite-strain from global mantle-circulation
 519 models: *Geophys. J. Int.*, 155, 696-714.
- 520 Bell, D.R., Rossman, G.R., Maldener, J., Endisch, D., Rauch, F., 2003, Hydroxide in olivine: A
 521 quantitative determination of the absolute amount and calibration of the IR spectrum: *J.*
 522 *Geophys. Res.*, 108, 2105, doi:10.1029/2001JB000679.
- 523 Birch, F., 1960, The velocity of compressional waves in rocks to 10 kilobars, 1: *J. Geophys.*
 524 *Res.*, 65, 1083-1102.
- 525 Birch, F., 1961, The velocity of compressional waves in rocks to 10 kilobars, 2: *J. Geophys.*
 526 *Res.*, 66, 2199-2224.
- 527 Bos, B., Spiers, C.J., 2001, Experimental investigation into the microstructural and mechanical
 528 evolution of phyllosilicate-bearing fault rock under conditions favouring pressure solution: *J.*
 529 *Struct. Geol.*, 23, 1187-1202.
- 530 Boudier, F., Coleman, R.G., 1981, Cross section through the peridotite in the Samail ophiolite,
 531 southeastern Oman mountains: *J. Geophys. Res.*, 86, 2573-2592.
- 532 Braun, M.G., 2004, Petrologic and microstructural constraints on focused melt transport in
 533 dunites and the rheology of the shallow mantle, MIT/WHOI Joint Program in Oceanography.
- 534 Braun, M.G., Hirth, G., Parmentier, E.M., 2000, The effects of deep damp melting on mantle
 535 flow and melt generation beneath mid-ocean ridges: *Earth Planet. Sci. Lett.*, 176, 339-356.
- 536 Cagnioncle, A.-M., Parmentier, E.M., Elkins-Tanton, L.T., 2007, Effect of solid flow above a
 537 subducting slab on water distribution and melting at convergent plate boundaries: *J.*
 538 *Geophys. Res.*, 112, B09402, doi:10.1029/2007JB004934.
- 539 Cammarano, F., Romanowicz, B., 2008, Radial profiles of seismic attenuation in the upper
 540 mantle based on physical models: *Geophys. J. Int.*, 175, 116-134.
- 541 Choblet, G., Parmentier, E.M., 2001, Mantle upwelling and melting beneath slow spreading
 542 centers: effects of variable rheology and melt productivity: *Earth Planet. Sci. Lett.*, 184, 589-
 543 604.
- 544 Conrad, C.P., Behn, M.D., Silver, P.G., 2007, Global mantle flow and the development of
 545 seismic anisotropy: Differences between the oceanic and continental upper mantle: *J.*
 546 *Geophys. Res.*, 112, B07317, doi:10.1029/2006JB004608.
- 547 Cooper, R.F., 2002, Seismic wave attenuation: Energy dissipation in viscoelastic crystalline
 548 solids, in Karato, S.-I., Wenk, H.-R., eds., *Plastic Deformation in Mineral and Rocks*;

- 549 Reviews of Mineralogy and Geochemistry Vol. 51: Washington, Mineralogical Society of
550 America, p. 253-290.
- 551 Craig, C.H., McKenzie, D., 1986, The existence of a thin low-viscosity layer beneath the
552 lithosphere: *Earth Planet. Sci. Lett.*, 78, 420-426.
- 553 Dasgupta, R., Hirschmann, M.M., 2006, Melting in the Earth's deep upper mantle caused by
554 carbon dioxide: *Nature*, 440, 659-662.
- 555 de Bresser, J.H.P., Peach, C.J., Reijs, J.P.J., Spiers, C.J., 1998, On dynamic recrystallization
556 during solid state flow: Effects of stress and temperature: *Geophys. Res. Lett.*, 25, 3457-
557 3460.
- 558 de Bresser, J.H.P., Ter Heege, J.H., Spiers, C.J., 2001, Grain size reduction by dynamic
559 recrystallization: can it result in major rheological weakening?: *Int. J. Earth Sci.*, 90, 28-45.
- 560 Dixon, J.E., Stolper, E., Delaney, J.R., 1988, Infrared spectroscopic measurements of CO₂ and
561 H₂O in Juan de Fuca Ridge basaltic glasses: *Earth Planet. Sci. Lett.*, 90, 87-104.
- 562 Drury, M.R., 2005, Dynamic recrystallization and strain softening of olivine aggregates in the
563 laboratory and the lithosphere, in Gapais, D., Brun, J.-P., Cobbold, P.R., eds., *Deformation
564 Mechanisms, Rheology and Tectonics: from Minerals to the Lithosphere*, Volume 243,
565 Geological Society of London, p. 143-158.
- 566 Dziewonski, A.M., Anderson, D.L., 1981, Preliminary reference Earth model: *Phys. Earth
567 Planet. Inter.*, 25, 297-356.
- 568 Evans, B., Renner, J., Hirth, G., 2001, A few remarks on the kinetics of static grain growth in
569 rocks: *Int. J. Earth Sci.*, 90, 88-103.
- 570 Evans, R.L., Hirth, G., Baba, K., Forsyth, D., Chave, A., Mackie, R., 2005, Geophysical evidence
571 from the MELT area for compositional controls on oceanic plates: *Nature*, 437, 249-252.
- 572 Faul, U.H., Jackson, I., 2005, The seismological signature of temperature and grain size
573 variations in the upper mantle: *Earth and Planet Sci. Lett.*, 234, 119-134.
- 574 Faul, U.H., Scott, D., 2006, Grain growth in partially molten olivine aggregates, *Contrib. Min.
575 Pet.*, 151, 101-111.
- 576 Freed, A.M., Bürgmann, R., 2004, Evidence of power-law flow in the Mojave desert mantle:
577 *Nature*, 430, 548-551.
- 578 Gaboret, C., Forte, A.M., Montagner, J.-P., 2003, The unique dynamics of the Pacific
579 Hemisphere mantle and its signature on seismic anisotropy: *Earth Planet. Sci. Lett.*, 208, 219-
580 233.
- 581 Gaherty, J.B., Jordan, T.H., Gee, L.S., 1996, Seismic structure of the upper mantle in a central
582 Pacific corridor: *J. Geophys. Res.*, 101, 22,291-22,309.
- 583 Goodwin, L.B., Wenk, H.-R., 1995, Development of phyllonite from granodiorite: Mechanisms
584 of grain-size reduction in the Santa Rosa mylonite zone, California: *J. Struct. Geol.*, 17, 689-
585 707.
- 586 Gribb, T.T., Cooper, R.F., 1998, Low-frequency shear attenuation in polycrystalline olivine:
587 Grain boundary diffusion and the physical significance of the Andrade model for viscoelastic
588 rheology: *J. Geophys. Res.*, 103, 27,267-27,279.
- 589 Gutenberg, A., 1948, On the layer of relatively low wave velocity at a depth of about 80
590 kilometers: *Bull Seis. Soc. Am.*, 58, 121-148.
- 591 Hager, B.H., 1991, Mantle viscosity—a comparison of models from postglacial rebound and
592 from the geoid, plate driving forces, and advected heat flux, in Sabadini, R., Lambeck,
593 K., Boschi, E., eds., *Glacial Isostasy, Sea Level and Mantle Rheology*: Dordrecht,
594 Netherlands, Kluwer Academic Publishers, p. 493-513.

- 595 Hall, C.E., Parmentier, E.M., 2003, Influence of grain size evolution on convective instability:
 596 *Geochem., Geophys., Geosys.*, 4, doi:10.1029/2002GC000308.
- 597 Harmon, N., Forsyth, D.W., Fischer, K.M., Webb, S.C., 2004, Variations in shear-wave splitting
 598 in young Pacific seafloor: *Geophys. Res. Lett.*, 31, doi:10.1029/2004GL020495.
- 599 Hauri, E.H., Gaetani, G.A., Green, T.H., 2006, Partitioning of water during melting of the Earth's
 600 upper mantle at H₂O-undersaturated conditions: *Earth Planet. Sci. Lett.*, 248, 715-734.
- 601 Hiraga, T., Anderson, I.M., Kohlstedt, D.L., 2003, Chemistry of grain boundaries in mantle
 602 rocks, *Am. Mineral.*, 88, 1015-1019.
- 603 Hirschmann, M.M., Aubaud, C., Withers, A.C., 2005, Storage capacity of H₂O in nominally
 604 anhydrous minerals in the upper mantle: *Earth Planet. Sci. Lett.*, 236, 167-181.
- 605 Hirth, G., Kohlstedt, D.L., 1996, Water in the oceanic upper mantle: implications for rheology,
 606 melt extraction and the evolution of the lithosphere: *Earth Planet. Sci. Lett.*, 144, 93-108.
- 607 Hirth, G., Kohlstedt, D.L., 2003, Rheology of the upper mantle and the mantle wedge: A view
 608 from the experimentalists, in Eiler, J., ed., *Inside the Subduction Factory*, Volume
 609 *Geophysical Monograph 138*: Washington, DC, AGU, p. 83-105.
- 610 Jackson, I., Fitz Gerald, J.D., Faul, U.H., Tan, B.H., 2002, Grain-size-sensitive seismic wave
 611 attenuation in polycrystalline olivine: *J. Geophys. Res.*, 107, 2360,
 612 doi:10.1029/2001JB001225.
- 613 Karato, S., 2003, Mapping water content in the upper mantle, in Eiler, J., ed., *Inside the*
 614 *Subduction Factory*, Volume *Geophysical Monograph 138*: Washington, DC, AGU, p. 135-
 615 152.
- 616 Karato, S., Toriumi, M., Fujii, T., 1980, Dynamic recrystallization of olivine single crystals
 617 during high temperature creep: *Geophys. Res. Lett.*, 7, 649-652.
- 618 Karato, S.-I., 1984, Grain-size distribution and rheology of the upper mantle: *Tectonophys.*, 104,
 619 155-176.
- 620 Karato, S.-I., 1989, Grain growth kinetics in olivine aggregates: *Tectonophys.*, 168, 255-273.
- 621 Karato, S.-I., 1995, Effects of water on seismic wave velocities in the upper mantle: *Proc. Japan*
 622 *Acad.*, 71, 61-66.
- 623 Karato, S.-I., Wu, P., 1993, Rheology of the upper mantle: A synthesis: *Science*, 260, 771-778.
- 624 Michael, P., 1995, Regionally distinctive sources of depleted MORB: Evidence from trace
 625 elements and H₂O: *EPSL*, 131, 301-320.
- 626 Minster, J.B., Anderson, D.L., 1980, Dislocations and nonelastic processes in the mantle: *J.*
 627 *Geophys. Res.*, 85, 6347-6352.
- 628 Minster, J.B., Anderson, D.L., 1981, A model for dislocation-controlled rheology for the mantle:
 629 *Phil. Trans. R. Soc. Lond. A*, 299, 319-356.
- 630 Montagner, J.-P., Tanimoto, T., 1991, Global upper mantle tomography of seismic velocities and
 631 anisotropies: *J. Geophys. Res.*, 96, 20,337-20,351.
- 632 Montési, L.G.J., Hirth, G., 2003, Grain size evolution and the rheology of ductile shear zones:
 633 from laboratory experiments to postseismic creep: *Earth Planet. Sci. Lett.*, 211, 97-110.
- 634 Nettles, M., Dziewonski, A.M., 2008, Radially anisotropic shear velocity structure of the upper
 635 mantle globally and beneath North America: *J. Geophys. Res.*, 113, B02303,
 636 doi:10.1029/2006JB004819.
- 637 Nishimura, C.E., Forsyth, D.W., 1989, The anisotropic structure of the upper mantle in the
 638 Pacific: *Geophys. J.*, 96, 203-229.

- 639 Parmentier, E.M., Turcotte, D.L., Torrance, K.E., 1976, Studies of finite amplitude non-
640 Newtonian thermal convection with application to convection in the Earth's mantle: *J.*
641 *Geophys. Res.*, 81, 1839-1846.
- 642 Parsons, B., Sclater, J.G., 1977, An analysis of the variation of ocean floor bathymetry and heat
643 flow with age: *J. Geophys. Res.*, 82, 803-827.
- 644 Peltier, W.R., 1998, Global glacial isostasy and relative sea level: Implications for solid earth
645 geophysics and climate system dynamics, in Wu, P., ed., *Dynamics of the Ice Age Earth*, p.
646 17-54.
- 647 Podolefsky, N.S., Zhong, S., McNamara, A.K., 2004, The anisotropic and rheological structure
648 of the oceanic upper mantle from a simple model of plate shear: *Geophys. J. Int.*, 158, 287-
649 296.
- 650 Poirier, J.-P., 1985, *Creep of Crystals*: Cambridge, Cambridge University Press.
- 651 Poirier, J.-P., Guillopé, M., 1979, Deformation induced crystallization of minerals: *Bull.*
652 *Mineral.*, 102, 67-74.
- 653 Pollitz, F.F., Sacks, I.S., 1996, Viscosity structure beneath northeast Iceland: *J. Geophys. Res.*,
654 101, 17,771-17,793.
- 655 Richards, M.A., Yang, W.-S., Baumgardner, J.R., Bunge, H.-P., 2001, Role of a low-viscosity
656 zone in stabilizing plate tectonics: Implications for comparative terrestrial planetology:
657 *Geochem. Geophys. Geosys.*, 2, doi:10.1029/2000GC000115.
- 658 Romanowicz, B., 1995, A global tomographic model of shear attenuation in the upper mantle: *J.*
659 *Geophys. Res.*, 100, 12375-12394.
- 660 Selby, N.D., Woodhouse, J.H., 2002, The Q structure of the upper mantle: constraints from
661 Rayleigh wave amplitudes: *J. Geophys. Res.*, 107, doi:10.1029/2001JB000257.
- 662 Spiegelman, M., Kelemen, P.B., 2003, Extreme chemical variability as a consequence of
663 channelized melt transport: *Geochem. Geophys. Geosys.*, 4, 1055,
664 doi:10.1029/2002GC000336.
- 665 Stein, C.A., Stein, S., 1992, A model for the global variation in oceanic depth and heat flow with
666 lithospheric age: *Nature*, 359, 123-129.
- 667 Stixrude, L., Lithgow-Bertelloni, c., 2005, Mineralogy and elasticity of the oceanic upper
668 mantle: Origin of the low-velocity zone: *J. Geophys. Res.*, 110, B03204,
669 doi:10.1029/2004JB002965.
- 670 Tan, B.H., Jackson, I., Fitz Gerald, J.D., 2001, High-temperature viscoelasticity of fine-grained
671 polycrystalline olivine: *Phys. Chem. Miner.*, 28, 641-664.
- 672 Tan, Y., Helmberger, D.V., 2007, Trans-Pacific upper mantle shear velocity structure: *J.*
673 *Geophys. Res.*, 112, B08301, doi:10.1029/2006JB004853.
- 674 Twiss, R.J., 1977, Theory and applicability of a recrystallized grain size paleopiezometer: *Pure*
675 *Appl. Geophys.*, 115, 227-244.
- 676 Urai, J.L., Means, W.D., Lister, C.S., 1986, Dynamic recrystallization of minerals, in Hobbs,
677 B.E.H., Hugh, C., eds., *Mineral and Rock Deformation: Laboratory Studies*, The Paterson
678 volume, Volume 36: *Geophys. Mono.*: Washington, D.C., American Geophysical Union.
- 679 Van der Wal, D., Chopra, P., Drury, M., Fitz Gerald, J., 1993, Relationships between
680 dynamically recrystallized grain size and deformation conditions in experimentally deformed
681 olivine rocks: *Geophys. Res. Lett.*, 20, 1479-1482.
- 682 Verma, R.K., 1960, Elasticity of some high density crystals: *J. Geophys. Res.*, 65, 757-766.

- 683 von Bagen, N., Waff, H.S., 1986, Permeabilities, interfacial areas and curvatures of partially
684 molten systems: Results of numerical computations of equilibrium microstructures: *J.*
685 *Geophys. Res.*, 91, 9261-9276.
- 686 Wark, D.A., Williams, C.A., Watson, E.B., Price, J.D., 2003, Reassessment of pore shapes in
687 microstructurally equilibrated rocks, with implications for permeability of the upper mantle:
688 *J. Geophys. Res.*, 108, 2050, doi:10.1029/2001JB001575.
- 689 Wolfe, C.J., Solomon, S.C., 1998, Shear-wave splitting and implications for mantle flow beneath
690 the MELT region of the East Pacific Rise: *Science*, 280, 1230-1232.
- 691 Zhao, Y.-H., Ginsberg, S.B., Kohlstedt, D.L., 2004, Solubility of hydrogen in olivine:
692 dependence on temperature and iron content: *Contrib. Min. Pet.*, 147, 155-161.
- 693

693 **Figure Captions**

694

695 **Figure 1.** **A)** Average S-wave velocity and **B)** radial anisotropy for oceanic regions from
 696 *Gaherty et al.* (1996) (G96) and *Nettles and Dziewonski* (2008) (ND08). **C)** Seismic Q factor
 697 from the models of *Dziewonski & Anderson* (1981) (PREM), *Romanowicz* (1995) (R95), and
 698 *Selby & Woodhouse* (2002) (SW02). Note the region of low S-wave velocity, low Q , and high
 699 radial anisotropy in the center of the asthenosphere at 100–200 km depth.

700

701 **Figure 2.** **A)** Model setup and **B)** imposed upper mantle temperature structure for plate ages of
 702 20, 60, and 120 Myrs assuming a mantle potential temperature of 1350°C.

703

704 **Figure 3.** Grain size as a function of stress calculated from the grain-size evolution models of
 705 *Hall & Parmentier* (2003) and *Austin & Evans* (2007) under **(A & B)** wet (1250°C, 600 H/10⁶Si)
 706 and **(C & D)** dry (1650°C, 50 H/10⁶Si) experimental conditions. Open circles and black triangles
 707 show the experimental data of *Van der Wal et al.* (1993) and *Karato et al.* (1980). Blue and red
 708 lines show model predictions for grain growth exponents (p_g) of 2 and 3, respectively. Multiple
 709 curves in **C & D** are for activation enthalpies of 200, 350, and 500 kJ/mol. All other parameters
 710 for grain growth under wet and dry conditions are given in Table 2.

711

712 **Figure 4.** Example calculation of grain size evolution in a 1-D channel flow model beneath a 60
 713 Myr plate moving at 10 cm/yr assuming a mantle potential temperature of 1350°C and an olivine
 714 water content of 1000 H/10⁶ Si. Model setup and solution follows *Podolefsky et al.* (2004), using
 715 the *Austin & Evans* (2007) model (Eq. 9) to solve for the **(A)** steady state grain size, d_{ss} and **(B)**
 716 composite mantle viscosity. Black, blue, and red curves show solutions with activation volumes
 717 for grain growth of 4, 8, and 12×10^{-6} m³/mol, respectively. Dashed and dash-dot curves show
 718 predictions of grain size from the piezometric relationships of *Karato et al.* (1980) and *Van der*
 719 *Wal et al.* (1993), respectively. **(C)** Calculated shear stress (dashed) and transition stress where
 720 $\dot{\epsilon}_{diff} = \dot{\epsilon}_{dist}$ (solid). Dislocation creep is the dominant deformation mechanism in regions where
 721 the calculated shear stress exceeds the transition stress. **(D)** Equilibration time for grain size to
 722 reach d_{ss} . Grey regions in all panels denote depths where $t_{eq} > 60$ Myr, and d_{ss} is not a good
 723 estimate of the true grain size.

724

725 **Figure 5.** **(A)** Steady state grain size and **(B)** mantle viscosity at a depth of 150 km and plate age
 726 of 60 Ma as a function of mantle potential temperature and water content. Calculations assume a
 727 plate velocity of 10 cm/yr and $V_g = 8 \times 10^{-6}$ m³/mol. Typical values of mantle temperature and
 728 olivine water content in the Earth's upper mantle (1300–1450°C and 50–2000 H/10⁶Si), result in
 729 grain sizes and viscosities in the range of 1–100 mm and $0.3\text{--}10 \times 10^{19}$ Pa·s, respectively.

730

731 **Figure 6.** Grain-size dependence of Q predicted by Eq. (13) compared to the attenuation data of
 732 *Tan et al.* (2001) and *Jackson et al.* (2002) (filled dots) at a fixed period of 8.2 s. Fit is achieved
 733 by adjusting p_Q , E_Q , and V_Q to best fit the data, holding p_{Qref} , E_{Qref} , and V_{Qref} constant to the values
 734 given by *Faul & Jackson* (2005).

735

736 **Figure 7.** **(A)** Grain size, **(B)** V_s , and **(C)** Q for a 60 Myr plate moving assuming olivine water
 737 contents of 50 (red) and 1000 (blue) H/10⁶ Si. Calculations assume a plate velocity of 10 cm/yr,

738 a mantle potential temperature of 1350°C and $V_g = 8 \times 10^{-6} \text{ m}^3/\text{mol}$. Black, dashed, and grey
 739 lines in **B** correspond to V_S models PA-5 (*Gaherty et al.*, 1996), ND08 (*Nettles & Dziewonski*,
 740 2008) for intermediate oceanic plate ages (25–100 Myr), and NF89 (*Nishimura & Forsyth*, 1989)
 741 for 52–110 Myr, respectively. Q models shown in **C** are same as in Figure 1C.

742
 743 **Figure 8.** (A) Grain size and (B) V_S as a function of plate age beneath a plate moving at a
 744 velocity of 10 cm/yr. Calculations assume a mantle potential temperature of 1350°C, an olivine
 745 water content of 1000 H/10⁶ Si, and $V_g = 8 \times 10^{-6} \text{ m}^3/\text{mol}$. Grey curve denotes depth above
 746 which t_{eq} is greater than the age of the plate. Black curves show V_S from *Nishimura & Forsyth*
 747 (1989) for 3 age intervals: 4–20 Myr, 20–52 Myr, and 52–110 Myr plotted at the center of each
 748 interval. (C) Grain size and (D) V_S as a function of depth for a plate age of 100 Myr. Blue and
 749 red curves show solutions for half-space cooling and plate models. Plate model assumes a plate
 750 thickness of 125 km. Grey region denotes depths where $t_{eq} > 100$ Myr. Black, dashed, and grey
 751 lines in **B** correspond to V_S models PA-5 (*Gaherty et al.*, 1996), ND08 (*Nettles & Dziewonski*,
 752 2008) for old oceanic plate ages (>100 Myr), and NF89 (*Nishimura & Forsyth*, 1989) for 52–110
 753 Myr, respectively.

754
 755 **Figure 9.** Total strain accumulated in the (A) dislocation creep and (B) diffusion creep regimes
 756 as a function of plate age. Model parameters are the same as Figure 8. (C) Grey area denotes
 757 portion of the upper mantle predicted to be anisotropic ($\dot{\epsilon}_{dist} > \dot{\epsilon}_{diff}$ and $\epsilon_{dist} > 1$). Red curves
 758 show the anisotropic parameter, $\xi = (V_{SH}/V_{SV})^2$, of *Nishimura & Forsyth* (1989) for 3 age
 759 intervals: 4–20 Myr, 20–52 Myr, and 52–110 Myr plotted at the center of each interval. Total
 760 accumulated (D) dislocation and (E) diffusion creep strain as a function of depth for a plate age
 761 of 100 Myr (blue curves). Dashed curve in **D** shows radial anisotropy for ocean plate ages >100
 762 Myr from *Nettles & Dziewonski* (2008). (F) Calculated shear stress (dashed) and transition
 763 stress where $\dot{\epsilon}_{diff} = \dot{\epsilon}_{dist}$ (solid) at a plate age of 100 Myr. Curves correspond to calculations for a
 764 dry (50 H/10⁶ Si, red) and wet (1000 H/10⁶ Si, dark blue) mantle as well as for the imposed
 765 grain size distribution of *Faul & Jackson* (2005) (light blue). Dislocation creep is the dominant
 766 deformation mechanism in regions where the calculated shear stress exceeds the transition stress.
 767 Note that for the *Faul & Jackson* (2005) grain size distribution most of the upper mantle above
 768 200 km is in the diffusion creep regime.

769
 770 **Figure 10.** (A,C) Grain size and (B,D) water content in olivine required to decrease V_S by 3% at
 771 70 km depth as a function of mantle temperature. Thin dashed lines show initial grain size, d_o ,
 772 and water content, COH_o , respectively. Red and blue curves in (A&C) show calculations for
 773 olivine water contents of 50 and 1000 H/10⁶Si, while red, blue, and black curves in (B&D)
 774 assume grain sizes of 1, 10, and 100 mm, respectively. Thick dark grey lines in (B&D) show
 775 water saturation in Fo₉₀ olivine calculated from *Zhao et al.* (2004). Grey region illustrates range
 776 of mantle temperatures between 50 and 70 km depth calculated from a half-space cooling model
 777 for a 100 Myr plate. Grey boxes in (A&B) show enlarged regions illustrated in (C&D).